J. Plasma Phys. (2026), *vol*. 92, E41
 doi:10.1017/S0022377826101482

Dissipation and particle acceleration at intermittent structures with velocity and magnetic shear: interaction of Kelvin–Helmholtz and drift–kink instabilities

Tsun Hin Navin Tsung[1,2], Gregory Werner[1], Dmitri A. Uzdensky[1,3] and Mitchell Begelman[2,4]

[1]Center for Integrated Plasma Studies, Physics Department, University of Colorado, 390 UCB, Boulder, CO 80309, USA

[2]JILA, University of Colorado and National Institute of Standards and Technology, 440 UCB, Boulder, CO 80309-0440, USA

[3]Rudolf Peierls Centre for Theoretical Physics, Clarendon Laboratory, University of Oxford, Parks Road, Oxford, OX1 3PU, UK

[4]Department of Astrophysical and Planetary Sciences, University of Colorado, 391 UCB, Boulder, CO 80309, USA

Corresponding author: Tsun Hin Navin Tsung, tsunhinnavin.tsung@colorado.edu

(Received 12 October 2025; revision received 30 January 2026; accepted 21 February 2026)

We present two-dimensional particle-in-cell simulations of a magnetised, collisionless, relativistic pair plasma subjected to combined velocity and magnetic field shear, a scenario typical at intermittent structures in plasma turbulence. We create conditions where only the Kelvin–Helmholtz instability (KHI) and drift–kink instability (DKI) can develop, while tearing modes are forbidden. The interaction of DKI and KHI generates qualitatively new structures, marked by a thickened shear layer with very weak electromagnetic field, modulated by KH vortices. Over a range of moderately strong velocity shears explored, the interaction of DKI and KHI results in a significant enhancement of dissipation over cases with only velocity shear or only magnetic shear. Moreover, we observe a new and efficient way of particle acceleration where particles are stochastically accelerated by the motional electric field exterior to the shear layer as they meander in an S-shaped pattern in and out of it. This process takes advantage of the bent geometry of the shear layer caused by the DKI–KHI interaction and is responsible for most of the highest-energy particles produced in our simulations. These results further our understanding of dissipation and particle acceleration at intermittent structures, which are present in plasma turbulence across a wide range of astrophysical contexts such as in active galactic nucleus jet sheaths, potentially relevant to limb-brightened emission, etc., and highlight the sensitivity of dissipation to multiple interacting instabilities, thus providing a strong motivation for further studies of their nonlinear interaction at the kinetic level.

Key words: Astrophysical Plasmas, Plasma Instabilities

1. Introduction

Intermittency, defined as the inherent spatiotemporal inhomogeneity of turbulence due to random fluctuations in the energy cascade as it proceeds from large to small scales (Zhdankin, Boldyrev & Uzdensky 2016), is generally present in astrophysical plasma turbulence. It manifests as thin structures with enhanced current densities and/or vorticities that take up a small fraction of space but account for a substantial portion of the energy dissipated in turbulence (Zhdankin *et al*. 2016). In a magnetised plasma, these structures imply strong velocity and magnetic shears coinciding in space. These two shears drive various instabilities. Thus, velocity shear is prone to the Kelvin–Helmholtz instability (KHI), which has been studied extensively using linear theory, fluid simulations and kinetic simulations. On the other hand, magnetic shear is susceptible to tearing modes and magnetic reconnection creating plasmoid chains and accelerating particles efficiently (Zenitani & Hoshino 2007; Guo *et al*. 2014; Werner *et al*. 2016; Sironi *et al*. 2025). Magnetic shear is also prone to drift–kink instability (DKI) (Zhu & Winglee 1996; Pritchett, Coroniti & Decyk 1996; Daughton 1999; Zenitani & Hoshino 2007, 2008; Barkov & Komissarov 2016; Werner & Uzdensky 2021) which, in a pair plasma with a weak guide magnetic field, grows faster during the linear stage than the tearing modes, but is generally not as efficient a particle accelerator as reconnection (Zenitani & Hoshino 2007). How the instabilities arising from velocity and magnetic shear interact with one another is an open question that has only now begun to be explored. A practical question is how such interaction affects energy dissipation and non-thermal particle acceleration. With applications to the boundaries of relativistic jets in active galactic nuclei in mind, Sironi, Rowan & Narayan (2021) considered a two-dimensional jet–wind model – a 'jet' medium made up of pair plasma and a 'wind' medium made up of normal (electron–ion) plasma with a relativistic velocity shear between them, and a magnetic field that was helical in the jet and toroidal and significantly weaker in the wind. That study found that KH vortices can wrap the field lines over each other, creating current sheets that trigger reconnection and considerable dissipation, but the specific set-up of that study precluded the authors from exploring the effects of DKI.

In this article we consider a similar computational set-up (see figure 1), but simplified in order to explore the joint effects of KH and DK modes, and their nonlinear interplay, on magnetic and bulk-kinetic dissipation. Here, for the first time, we incorporate the effects of velocity and magnetic shear in a two-dimensional configuration where DKI coexists with KHI, while tearing is forbidden. Using first-principles particle-in-cell (PIC) simulations, we show that the interaction between the KHI and DKI creates qualitatively new structures and very different amounts of dissipation compared with the case when only one of the instabilities is present. It also leads to a new and efficient means of non-thermal particle acceleration. Thus, dissipation is highly sensitive to the interplay of the two instabilities.

The structure of this paper is as follows. In § 2 we describe the simulation set-up for this study, including the parameters explored and the diagnostics used. In § 3 we present our results, focusing first on the morphology and dissipation of the system in § 3.1 and then on particle acceleration in § 3.2. In § 4 we discuss the applicability of our results and draw our conclusions.

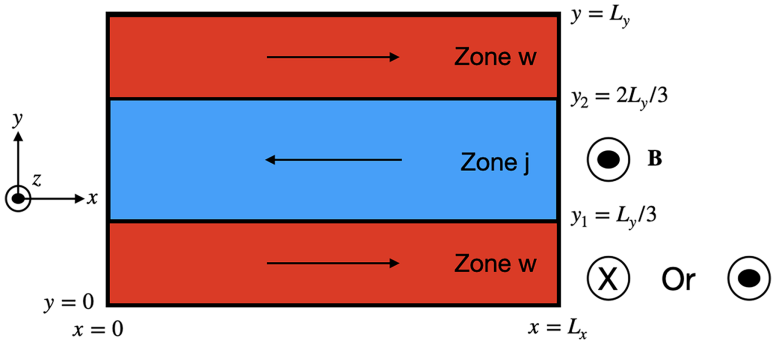

FIGURE 1. The double-shear-layer set-up used in this study, consisting of two zones, Zone j and Zone w, in equal and opposite motion along the x axis with respect to each other. The magnetic field in Zone j points out of the page ($+z$ direction) while that in Zone w can point either into ($-z$) or out of the page. The plasma quantities B, E, etc., are connected smoothly between the two zones by a tanh profile (equation (A2)).

2. Methods

We perform two-dimensional relativistic electromagnetic PIC simulations using the code Zeltron (Cerutti *et al.* 2013). We consider a relativistically warm ($\theta \equiv T/m_e c^2 \sim 1$) electron–positron pair plasma in a double-layer shear flow (see figure 1). Our set-up consists of two regions, Zone j (blue) and Zone w (red), with two thin interface layers between them. In the following, x is the direction of the fluid flow while y is the gradient direction. We impose an initial out-of-plane magnetic field that is perpendicular to the flow and the gradient direction, i.e. $\boldsymbol{B} = B(y)\hat{z}$. We simulate the x, y plane keeping all three components for vector quantities. Since the z direction is not simulated, no tearing modes can be excited (a full three-dimensional study is left to future work). This allows us to focus on the KH and DK modes and their interplay. We run the simulations in the frame where both zones are moving at the same speed but in opposite ($\pm\hat{x}$) directions.

The set-up is characterised by the following initial dimensionless parameters: Zone j's bulk-flow 4-velocity $u_j = \Gamma_j \beta_j$, normalised temperature $\theta_j = T_j/m_e c^2$, magnetisation $\sigma_j = B_j^2/4\pi w_j$ (where w_j is Zone j's relativistic enthalpy density) and the ratio of Zone w's to Zone j's magnetic field B_w/B_j. Zone j's magnetisation σ_j and normalised temperature θ_j are set to 1 initially in all the cases we consider, while u_j is varied from run to run. Zone w's rest-frame density, temperature and bulk speed are initially set equal to those in Zone j (with bulk velocity reversing direction). We connect Zone j's and Zone w's flow velocities and magnetic fields smoothly by a tanh function[1] of y with a transition half-width Δ (equation (A2)). Combining Maxwell's equations and the ideal gas law with the assumptions of pressure balance across the shear layer and the ideal magnetohydrodynamic (MHD) condition that the initial electric field is purely motional, $\boldsymbol{E} = -\boldsymbol{v} \times \boldsymbol{B}/c$, the y profiles of the electric field, velocity, density and temperature of the electrons and positrons can be determined. The initial velocities of

[1] This magnetic field configuration is Harris-like (Harris 1962), but we have modified the plasma density profile of the classic Harris-sheet set-up substantially to accommodate a non-zero relativistic bulk plasma flow; see Appendix A for details.

Identifier	σ_j	θ_j	u_j	B_w/B_j
Mixed-shear case (0.01, −1)	1	1	0.01	−1
Mixed-shear case (0.03, −1)	1	1	0.03	−1
Mixed-shear case (0.05, −1)	1	1	0.05	−1
Mixed-shear case (0.07, −1)	1	1	0.07	−1
Mixed-shear case (0.1, −1)	1	1	0.1	−1
Mixed-shear case (0.2, −1)	1	1	0.2	−1
Mixed-shear case (0.3, −1)	1	1	0.3	−1
Mixed-shear case (0.4, −1)	1	1	0.4	−1
Mixed-shear case (0.5, −1)	1	1	0.5	−1
Mixed-shear case (0.6, −1)	1	1	0.6	−1
Mixed-shear case (0.7, −1)	1	1	0.7	−1
Mixed-shear case (0.8, −1)	1	1	0.8	−1
Mixed-shear case (0.9, −1)	1	1	0.9	−1
VS case	1	1	0.5	+1
MS case	1	1	0	−1

TABLE 1. Simulation parameters for the cases explored in this study. Here, $\sigma_j \equiv B_j^2/4\pi w_j$ and $\theta_j \equiv T_j/m_e c^2$ are the initial magnetisation and the initial relativistic temperature, respectively, in Zone j, while $u_j \equiv \Gamma_j \beta_j$ is the bulk 4-velocity of the plasma flow in Zone j and B_w/B_j is the ratio of Zone w's to Zone j's magnetic field (+1 means they are aligned, −1 means they are oppositely aligned).

the particles are then sampled from the local drifting Maxwell–Jüttner distribution. Details of this set-up can be found in Appendix A. With this set-up, we ran two control cases with only one type of shear present $(u_j, B_w/B_j) = (0.5, +1)$ and $(0, -1)$ (hereafter referred to as the VS and MS cases, respectively), and a series of mixed cases with fixed magnetic shear $(B_w/B_j = -1)$ and progressively varied $u_j : \{0.01, 0.03, 0.05, 0.07, 0.1, 0.2, 0.3, 0.4, 0.5, 0.6, 0.7, 0.8, 0.9\}$. This allowed us to investigate systematically the effects of velocity shear on DKI and its co-evolution with KHI. Table 1 presents a summary of the simulation parameters used.

The simulation domain is a rectangular box with periodic boundaries spanning $L_x = 100 d_{e,j}$ in the x direction and $L_y = 300 d_{e,j}$ in the y direction, where $d_{e,j} \equiv (\bar{\gamma}_j m_e c^2/4\pi \tilde{n}_{e,j} e^2)^{1/2}$ is the electron inertial length in Zone j; it is resolved fiducially by 1024×3072 grid cells, which resolves Zone j's electron inertial length $d_{e,j}$ by $\approx$10 cells. The initial half-thickness of each shear layer, located at $y_{1,2} = \{L_y/3, 2L_y/3\} = \{100, 200\}\, d_{e,j}$, is set to $\Delta = 5 d_{e,j}$ as motivated by Serrano, Nättilä & Zhdankin (2024), which finds that intermittent structures typically have a width of $3 d_{e,j}$. For relativistically warm ($\theta \sim 1$), moderately magnetised ($\sigma \sim 1$) pair plasma, Zone j's electron Debye length $\lambda_{\mathrm{D},e}$, average gyroradius $\rho_{e,j}$ and electron inertial length $d_{e,j}$ are roughly equal, so all the kinetic scales are well resolved (exact definitions for $d_{e,j}$, $\lambda_{\mathrm{D},e}$ and $\rho_{e,j}$ are given in Appendix B, though we note that $\rho_{e,j} \sim (\theta_j/\sigma_j)^{1/2} d_{e,j}$). We create 64 particles per cell (PPC) per species (totaling 128 PPC); this results in $d_{e,j}^2/\Delta x \Delta y \times \mathrm{PPC} \sim 6400$ particles per area spanned by Zone j's electron inertial length, sufficient for our purposes. We run our simulations for approximately $50 L_x/c$ to ensure the saturated stage is reached. For kinetic diagnostic purposes, we randomly select and track the trajectories of 10^5 electrons and positrons throughout the simulation.

The main focus of this study is on the evolution of the total magnetic and bulk kinetic energies. The total magnetic energy is calculated as $E_B \equiv \int B^2/8\pi \, \mathrm{d}V$. To calculate the total bulk kinetic energy, we first perform a Lorentz transformation into the local zero-particle-flux (Eckart) frame at each cell, calculate the local pressure tensor there and then subtract it from the total stress tensor to obtain the bulk-flow stress tensor. Integrating its trace over the box volume gives the total bulk kinetic energy E_{KE} [details of this procedure are given in Appendix C (V. Zhdankin, personal communication)]. As a consistency check, the total energy in all our simulations is conserved to within 0.2 %.

3. Results

3.1. *Morphology and dissipation*

In this section, we first give a quick overview of the evolution of selected simulations, summarising the stages they go through; then we discuss each stage in greater detail, focusing on the linear growth rate, nonlinear shear-layer width and dissipation.

Figure 2 shows the typical evolution of our simulations, which first follows a linear stage, then a nonlinear stage when the conversion of magnetic or bulk kinetic energy into internal energy takes place and finally a saturated stage. The onset times of these stages are different for the MS, mixed-shear and VS cases. In the MS case, the linear stage occurs at $0 < tc/L_x \lesssim 2.5$, the nonlinear stage at $2.5 \lesssim tc/L_x \lesssim 13$ and the saturated stage from $tc/L_x \gtrsim 13$. For the mixed-shear cases, the linear stage ends roughly at $tc/L_x \approx 2.5$, as in the MS case, but the nonlinear stage is somewhat prolonged, lasting until $tc/L_x \approx 25$ before transitioning to the saturated stage. For the VS case, the linear stage ends at $tc/L_x \approx 7$, the nonlinear stage lasts until $tc/L_x \approx 13$ and is then followed by the saturated stage. The upper two panels of figure 2 show the evolution of the two control cases: the VS case ($B_j/B_w = 1$), where only the KHI is excited, and the MS case ($u_j = 0$), where only the DKI is excited. The instabilities give rise to prominent features in the nonlinear stage: cat's-eye vortices can be clearly seen in the VS case (upper-top panel of figure 2), while Rayleigh–Taylor-like plume features (upper-middle panel of figure 2) arise in the MS case. The nonlinear phase begins when the y displacement of the features becomes comparable to the modal wavelength in the x direction. For the VS case this is characterised only by a slight smearing of the KH vortices, while the DK plumes mix together violently. This is the stage where most of the dissipation (if any) occurs. In the later saturated stage, the KH vortices persist to the end in the VS case, while in the MS case the mixing leads to a thickened shear layer where the electric and magnetic fields are drastically reduced. The DK plumes do not persist to the end.

When both types of shear are present, the KHI and DKI interact. The nonlinear stage ($tc/L_x \gtrsim 5{-}6$) is marked by the nonlinear interactions of the KH vortices and DK plumes, creating a turbulent shear layer (e.g. upper-bottom panel of figure 2) at around $(7{-}10)L_x/c$ (a small multiple of the DK growth time scale). As discussed below, the dissipation level is also modified significantly. In the saturated stage, the turbulence subsides, giving way to a shear layer consisting of a broad 'annihilated core' where the E and B fields are suppressed, the flow is nearly stagnant and the thermal pressure dominates. This relatively quiet layer is enshrouded by an active 'KH cocoon' (lower panel of figure 2).

To examine how velocity shear modifies the linear growth rate of the DKI, we calculate the deviation of the z-component magnetic field from the initial value, i.e. $\delta B_z = B_z(x, y, t) - B_z(x, y, 0)$, at $y/d_{e,j} = 200$ (which is the initial location of the

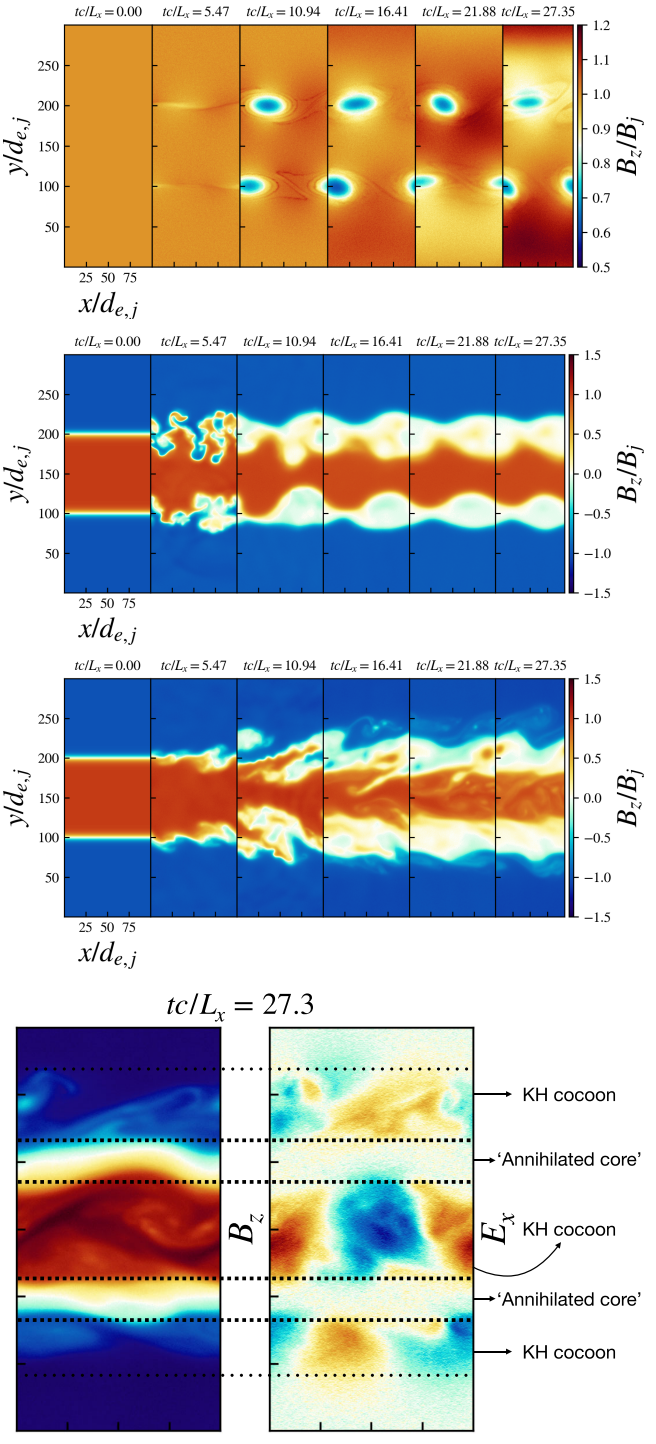

FIGURE 2. Snapshots of B_z/B_j for simulations with velocity shear only ('VS', upper-top), magnetic shear only ('MS', upper-middle) and both shears ($u_j = 0.5$, $B_w/B_j = -1$, upper-bottom). The lower panel shows snapshots of B_z, E_x in the saturated stage ($tc/L_x = 27.3$) for the $u_j = 0.5$, $B_w/B_j = -1$ case, with the 'annihilated core' and 'KH cocoon' annotated.

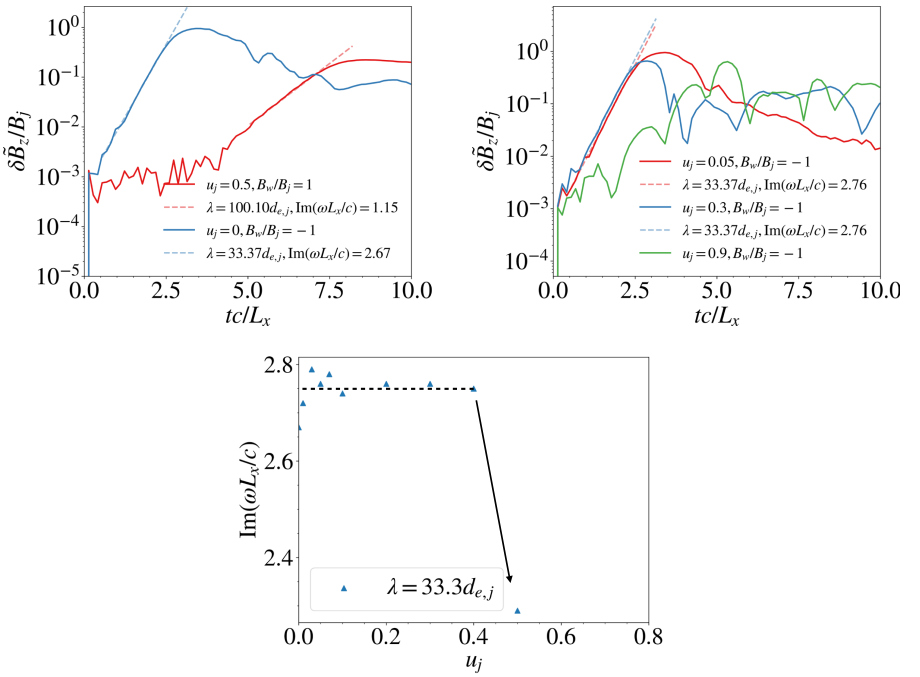

FIGURE 3. Top left: growth curves of selected modes (indicated by the wavelength λ) for the control cases (red for VS, blue for MS). Note that the wavelengths of the displayed modes are different for the MS ($\lambda = 33 d_{e,j}$) and VS ($\lambda = 100 d_{e,j}$) cases. Top right: growth curves for selected mixed-shear cases (red for $u_j = 0.05$, blue for $u_j = 0.3$, green for $u_j = 0.9$). In both panels, dashed lines show fitted linear growth rates as indicated in the legends. The growth curve of the $u_j = 0.9$ case is not fitted as no exponential growth phase can be identified. Bottom: fitted linear growth rates for mixed-shear cases as a function of $u_j \equiv \Gamma_j \beta_j$, with the fastest-growing mode displayed in the legend. No fitted growth rate is displayed for the $u_j > 0.6$ cases as no exponential growth phase can be identified. Note that the growth rate of the VS case is not displayed in this panel. The black arrow highlights the drastic drop in growth rate for the $u_j = 0.5$ case.

upper shear layer) and then Fourier-transform it in the x direction, i.e. compute $\delta\tilde{B}_z(k_x, t)$. We then select for our analysis the Fourier mode whose amplitude first reaches $\delta\tilde{B}_z/B_j = 0.1$ (which is typically $\lambda \approx 33 d_{e,j}$ for the MS and mixed-shear cases and $\lambda \approx 100 d_{e,j}$ for the VS case, or equivalently $k_x \Delta \sim 1$, where Δ is the initial shear-layer width, as shown in figure 3). The variation of $\delta\tilde{B}_z/B_j$ of this mode with time (in units of tc/L_x) is displayed in figure 3. We observe, for most cases (VS, MS and the $u_j < 0.6$ cases), a clear linear phase, exponential growth within the first $2.5 L_x/c$. For the VS and MS cases (top-left panel), two very different growths can be seen, corresponding to the KH-only (red line, VS) and DK-only (blue line, MS) instabilities. Using (25) in Zenitani & Hoshino (2007) to estimate the growth rate of the relativistic DKI in the MS case, we find an analytic expectation of Im$(\omega L_x/c) \approx 3.05$, fairly consistent with our measured simulation result[2] Im$(\omega L_x/c) \approx 2.67$. Adopting

[2]The analytic growth rate of DKI used in this comparison assumes a two-fluid model, an adiabatic index of 4/3, a mode wavelength long compared with the initial shear-layer thickness and negligible gyroviscosity (see

the linear analysis described in Chow *et al*. (2023), we calculate the analytic growth rate for the KHI to be $\mathrm{Im}(\omega L_x/c) \approx 2.47$ for the VS case, whereas our simulation result gives $\mathrm{Im}(\omega L_x/c) = 1.15$, which is a factor of 2 lower. Possible reasons for this discrepancy are noted in a footnote.[3] Even though the KH and DK modes separately grow on different time scales and length scales, as shown in the top-left panel for the VS and MS cases, there is only one linear, exponential growth phase in the mixed-shear cases ($u_j \neq 0$, $B_w/B_j = -1$), as shown in the top-right panel (e.g. red and blue lines). From figure 3, the linear stage for this mode lasts for $2.5L_x/c$ for the MS case and all the mixed-shear cases with $u_j < 0.4$, whereas for the VS case it lasts until about $7L_x/c$. When u_j is increased above 0.5, no exponential growth phase can be identified.

We extract the growth rates by fitting the linear phase whenever it can be identified and plot the results as a function of u_j in the bottom panel of figure 3. The wavelength of the displayed mode is $\lambda = 33.3d_{e,j}$ (note that only the MS and mixed-shear cases are displayed in this panel). As shown in this panel, the growth rates of all cases with an identifiable linear growth phase (except the $u_j = 0.5$ case) are roughly the same [$\mathrm{Im}(\omega L_x/c) \sim 2.75$, equivalently $\mathrm{Im}(\omega/\omega_{pe,j}) \sim 0.0275$ and $\mathrm{Im}(\omega/\omega_{ce,j}) \sim 0.0138$], equal to that in the MS case. This, together with the fact that the fastest-growing modes for the mixed-shear cases are the same as in the MS case, implies that the DK modes still dominate the linear growth in the presence of moderately strong velocity shear ($u_j \lesssim 0.4$), and there is minimal interaction of the DK and KH modes in this linear stage. The effect of velocity shear in the linear phase becomes more apparent for $u_j \geqslant 0.5$ – the growth rate drops to $\mathrm{Im}(\omega L_x/c) \sim 2.29$ for $u_j = 0.5$ and no exponential growth phase can be identified for stronger shears.

Despite the relatively unchanged linear growth rates observed at early times for $u_j \lesssim 0.4$ cases, the morphological changes at late times are apparent. In the following, we characterise the structure of the test cases by the width of the thickened shear layer. In the left-hand panel of figure 4 we plot the x-averaged profiles of B_z/B_j at the final time $tc/L_x = 55$ for several values of u_j. We observe that turbulence driven by nonlinear interactions of the instabilities has thickened the shear layer, within which B_z is reduced. We measure the width of this layer Δy_{B_z} at $tc/L_x = 55$ by the y separation between isosufaces of $B_z/B_j = -0.5$ and 0.5 and display it as a function of u_j in the right-hand panel of figure 4. A non-trivial picture emerges. The width is substantial in the pure DKI MS case ($u_j = 0$), but decreases with increased shear for relatively weak $u_j \lesssim 0.1$. It then bounces back up for intermediate values of

Daughton (1999) for why it could be important). In fact, Zenitani & Hoshino (2007) found that the analytic formula overestimates the simulated growth rate as well, by a margin consistent with what we observe. For completeness, the DKI growth rate in the long-wavelength limit found by Zenitani & Hoshino (2007) is $\gamma_{\mathrm{DKI}} = [1 - \Gamma(\theta_e^{-1} + 4)\beta^2 k_x \Delta]\beta k_x \Delta/\tau_c$, where $\tau_c \equiv \Delta/c$, Γ is the bulk Lorentz factor and β is the drift speed of either species.

[3] The analytic growth rate of the KHI used in this comparison assumes a razor-thin transition layer, an adiabatic index of 4/3 and the relativistic MHD equations (Chow *et al*. 2023). Even though the growth rate is derived assuming MHD, Che & Zank (2023) showed in the non-relativistic limit that the electron-scale KHI has a growth rate equation that is almost identical in form to that derived assuming ideal MHD, but using the electron mass for all mass quantities (e.g. $m \to m_e$, $\rho \to \rho_e$, etc., such that the growth time scale is also much faster, on the electron gyroperiod). Thus, we formulate our baseline growth rate for comparison by employing the growth rate results derived in Chow *et al*. (2023) for relativistic MHD, using the electron mass for all mass quantities. The factor of 2 difference in the growth can be attributed to the fact that (i) the growth rate evaluated from a razor-thin shear-layer model typically overestimates the actual growth rate in simulations with finite shear-layer thickness and (ii) the growth rate derived in Chow *et al*. (2023) assumes an electron–ion plasma, while a pair plasma should incur an order unity difference. Thus the difference observed is not unexpected.

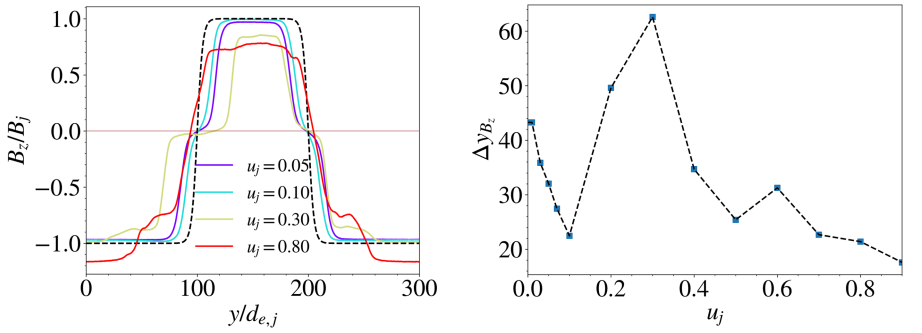

FIGURE 4. Left: x-averaged plots of B_z/B_j for $u_j = 0.05, 0.1, 0.3, 0.8$, $B_w/B_j = -1$ at $tc/L_x = 55$, showing how the instabilities thicken the magnetic shear layer. The black dashed line is the x-averaged plot of B_z/B_j at $t = 0$. The horizontal translucent brown line indicates $B_z = 0$. Right: width of the thickened shear layer as a function of velocity shear, at $tc/L_x = 55$.

u_j ($0.1 < u_j < 0.3$), but drops again for larger values of u_j. This is quite different from the u_j dependence of the linear growth rate, which shows no such variations for $u_j \lesssim 0.4$. We therefore attribute the changes in the shear-layer width to nonlinear interaction of the instabilities. Namely, when the velocity shear is moderately weak ($u_j < 0.1$), DK plumes protruding across the plasma's bulk flow are quickly sheared away, reducing the layer's width. As u_j increases to around 0.2, KHI initiates and the cat's-eye vortices wrap up the layer, causing it to thicken again. When the velocity difference becomes super-magnetosonic, however, KHI is suppressed (Chow *et al.* 2023), leading to a thinner saturated layer. We observe that the onset of KH vortices, if it happens, occurs at a slightly later time than the linear, DK-dominated growth phase. For example, in the $u_j = 0.3$ case, the KH vortices set in at around $tc/L_x \sim 5$, whereas the linear phase occurs in the range $0 < tc/L_x < 2.5$ (observe in the top-right panel of figure 3 that there is a small increase in $\delta\tilde{B}_z/B_j$ at $tc/L_x \sim 5$ for the blue line, indicative of KH vortex wrap-ups). As shown below, the width of the thickened shear layer correlates strongly with magnetic energy dissipation.

The dissipation of magnetic and bulk kinetic energy is closely tied to the instabilities. In the top- and bottom-left panels of figure 5 we show the evolution of the total magnetic and bulk kinetic energies, E_B and E_{KE}, normalised by their initial values, for selected cases. Most of the dissipation occurs at around $tc/L_x \approx 10$, when the perturbations have fully grown, with E_B and E_{KE} steadying out afterwards. Up to half of the initial E_B and E_{KE} can be dissipated as a result of the instabilities, but as shown in the top- and bottom-right panels of figure 5, this is very sensitive to the velocity shear u_j. In fact, the dissipation of magnetic energy for different u_j closely mimics the trend for the width of the thickened shear layer. The reason for this is simple: the shear layer is devoid of magnetic flux density, whereas outside the layer it is roughly the same as the initial value, so the total decrease of magnetic energy is just due to dissipation of the field inside this layer. This is why the decrease in E_B is directly proportional to the unmagnetised layer's thickness Δy_{B_z}. The dissipation of bulk kinetic energy also shows a prominent peak at moderate velocity shears $0.2 < u_j < 0.4$, but unlike E_B, the dissipation of E_{KE} is less effective for weak velocity shears $u_j < 0.1$. We note also that the case with only velocity shear (VS) exhibits zero magnetic dissipation and close-to-zero (less than 5 %) bulk kinetic energy dissipation. While KH vortices alone do not appear to be able to dissipate magnetic

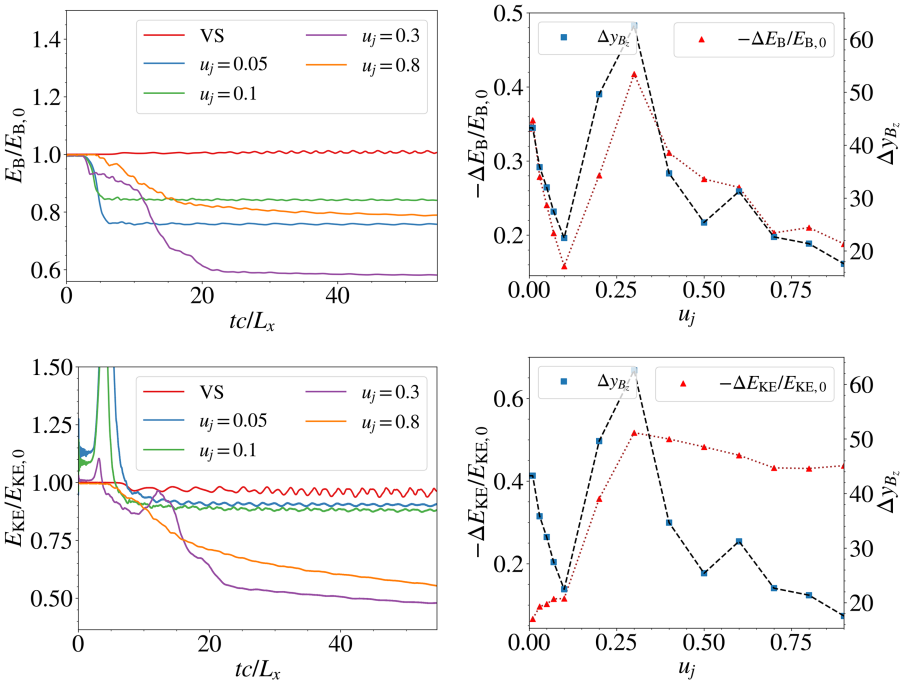

FIGURE 5. Top and bottom left: the total magnetic and bulk kinetic energies within the simulation box E_B, E_{KE}, normalised by their initial values $E_{B,0}$, $E_{KE,0}$, against time for selected cases ($u_j = 0.05$, 0.1, 0.3, 0.8, $B_w/B_j = -1$ and the VS case). Top and bottom right: brown dotted lines with red triangles show the magnetic and bulk kinetic energy dissipated, measured by $-\Delta E_B/E_{B,0}$, $-\Delta E_{KE}/E_{KE,0}$, as a function of velocity shear u_j, at $tc/L_x = 50$. Black dashed lines with blue squares show the width of the thickened shear layer for different u_j, same as the bottom-right panel of figure 4, superimposed for comparison. Here, $u_j \equiv \Gamma_j \beta_j$.

energy or bulk kinetic energy effectively in this two-dimensional configuration (at least within the time scales we explored), and even a weak velocity shear is enough to reduce the dissipation of magnetic energy with DK plumes alone, their combined effects are strong. There are two noteworthy points here: firstly, that the dissipation correlates with the thickening of the shear layer and, secondly, that the instabilities can synergistically increase the dissipation. With two shears, which could source two different instabilities, it is possible for one type of shear to limit how large the perturbations arising from the other type can grow, thus reducing dissipation; e.g. velocity shear disrupts DK plumes. At the same time, it is also possible for one type of shear to enhance the dissipative effect of perturbations arising from the other type of shear, as in the case of magnetic shear influencing KH vortices.

We summarise our discussion up to this point with a schematic diagram (figure 6), showing how the flow structure and dissipation change with respect to the magnitude of the two shears we investigated, within the regimes we explored. As shown in the diagram, there are two free parameters, each controlling a type of shear, represented by the two axes. We show simulation snapshots for selected cases, each characterised by a combination (u_j, B_w/B_j). In the absence of any shear ($u_j = 0$, $B_w/B_j = +1$), the result is just particle white noise. In the absence of magnetic shear (VS case; $B_w/B_j = +1$), KH vortices develop when the velocity shear increases, subsiding

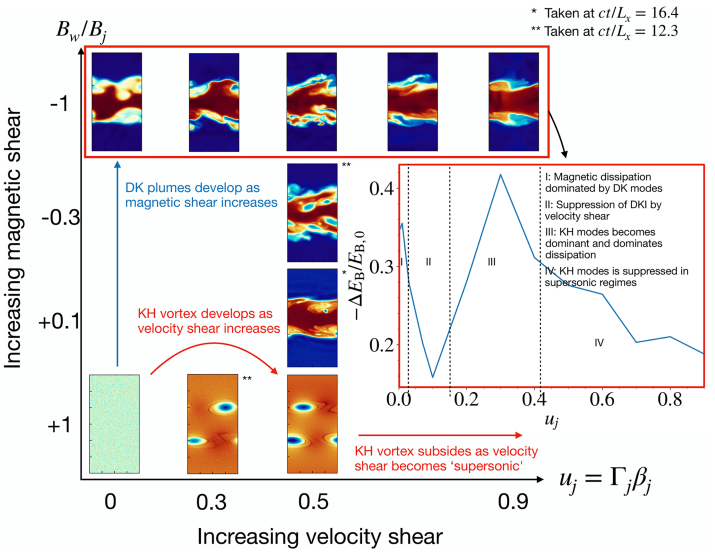

FIGURE 6. Schematic diagram showing how velocity and magnetic shear affect the plasma flow through the instabilities they excite, with the magnitude of the velocity shear (measured by u_j, the 'jet' 4-velocity) on one axis and the magnetic shear (measured by B_w/B_j) on the other. The snapshots are taken mostly at $tc/L_x = 8.2$, with some taken at other times. The inset shows the fraction of magnetic energy dissipated as a function of u_j (measured by $-\Delta E_B/E_{B,0}$, same as figure 5) for the cases framed in red. The plot is divided into four regions, representing different regimes where a certain instability is active/suppressed.

when u_j becomes supersonic (Chow *et al*. 2023). In the absence of velocity shear (MS case; $u_j = 0$, $B_w/B_j = -1$), Rayleigh–Taylor-like plumes develop from DKI, developing into a thickened shear layer with subdued electromagnetic field. Holding the velocity shear constant at $u_j = 0.5$, we observe an increase in turbulent activity as the magnetic shear B_w/B_j increases, indicating enhanced nonlinear interplay between the KHI and DKI. With the magnetic shear fixed at $B_w/B_j = -1$ while varying u_j, which is the subject of inquiry in this study, we observe the aforementioned change in morphology and dissipation. These changes can be divided into four regimes: (i) without velocity shear, magnetic dissipation is dominated by the DK modes; (ii) in the presence of a weak velocity shear, the DK plumes are suppressed nonlinearly by the velocity shear, resulting in a drop in dissipation; (iii) with a moderately strong velocity shear, KH vortices are excited, resulting in nonlinear interplay with the DK modes, leading to enhanced dissipation; and (iv) with supersonic shear, KH modes subside and dissipation reduces.

3.2. *Particle acceleration*

We now delve deeper into the kinetic aspects of the instabilities and dissipation by tracking particles that have been accelerated. We first point out the generation of a non-thermal tail in the mixed-shear ($u_j = 0.3$, $B_w/B_j = -1$) case in figure 7, showing a small power-law section for $3 \leqslant \gamma \leqslant 30$ with spectral index ~ 2.3 and a steeper spectrum for $30 \leqslant \gamma \leqslant 200$, suggestive of a scale-invariant dissipative process. We also observe a modest power-law tail at $3 \leqslant \gamma \leqslant 30$ with spectral index ~ 2.3 in the MS case, followed by a much steeper power law and then a pile-up of

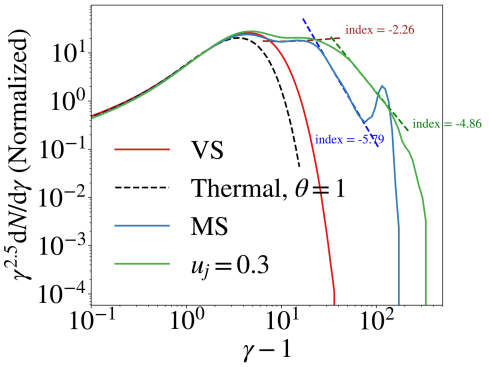

FIGURE 7. Particle energy distributions for the VS, MS and $u_j = 0.3$, $B_w/B_j = -1$ cases at $tc/L_x = 27.3$, showing the generation of a non-thermal power-law-like tail. For comparison, a thermal (Maxwell–Jüttner) distribution with temperature $\theta = 1$ is shown with a black dashed line. Also shown are three power-law segments at parts of the curves that resemble a power law, denoted by brown, green and blue dashed lines, corresponding to, respectively, power-law indices of –2.26, –4.86 and –5.79.

particles at $\gamma \sim 10^2$. The pile-up is similar to that observed in figure 14 of Zenitani & Hoshino (2007). The energy distribution of the VS case remains thermal. In the top panels of figures 8–10 we show, respectively, for the VS, MS and mixed ($u_j = 0.3$, $B_w/B_j = -1$) cases, the Lorentz factors of selected electrons as a function of time in comparison with the work done on them by various components of the electric field; the three bottom panels in each case display the trajectories of the particles during three time windows, taken in the linear, nonlinear and saturated stages. Additional explanatory panels are also inserted. In the top panel of each figure, the blue solid line denotes the Lorentz factor $\gamma(t)$ of the particle, while the orange dashed line denotes the work done by the ideal MHD, motional electric field, $W_{\rm ideal}(t) = -e\int_0^t \boldsymbol{E}_{\rm ideal}\cdot\boldsymbol{v}\mathrm{d}t'/m_ec^2$; the green dashed line denotes work done by the E_x component, $W_x(t) = -e\int_0^t E_x v_x \mathrm{d}t'/m_ec^2$; and the red dashed line denotes the work done by the E_y component, $W_y(t) = -e\int_0^t E_y v_y \mathrm{d}t'/m_ec^2$. In each of the bottom panels, the particle's trajectory is displayed by a rainbow-coloured line with the progress of time shown in the colourbar (blue, earlier; red, later). The particle trajectories are overlaid on three simulation snapshots of E_x to show the background field through which the particle is passing.

For the VS case (figure 8), we select a particle that has reached a Lorentz factor of 10 at $tc/L_x = 27.4$ for display. As observed in the top panel, the Lorentz factor of this particle remains at $\gamma \sim 10$ throughout the simulation; it does not experience net acceleration over time. There is no substantial work done by the ideal motional E field. The work done by E_x and E_y is anti-correlated and exhibits short and long periodicity on the time scales of $\sim L_x/c$ (short) and $10L_x/c$ (long). In the bottom panels, which trace the trajectory of the particle at three time windows, we observe that the particle is initially undergoing $E \times B$ drift (bottom-left panel). When KH vortices develop, the background E field changes, bending the drift's trajectory (bottom-middle panel). The particle goes back and forth between two vortices with different field polarities in ellipsoidal motion, gaining and losing the same amount of energy as it passes through them. This leads to the short periodicity in the E_x and E_y work done. The particle maintains its ellipsoidal motion throughout the rest of

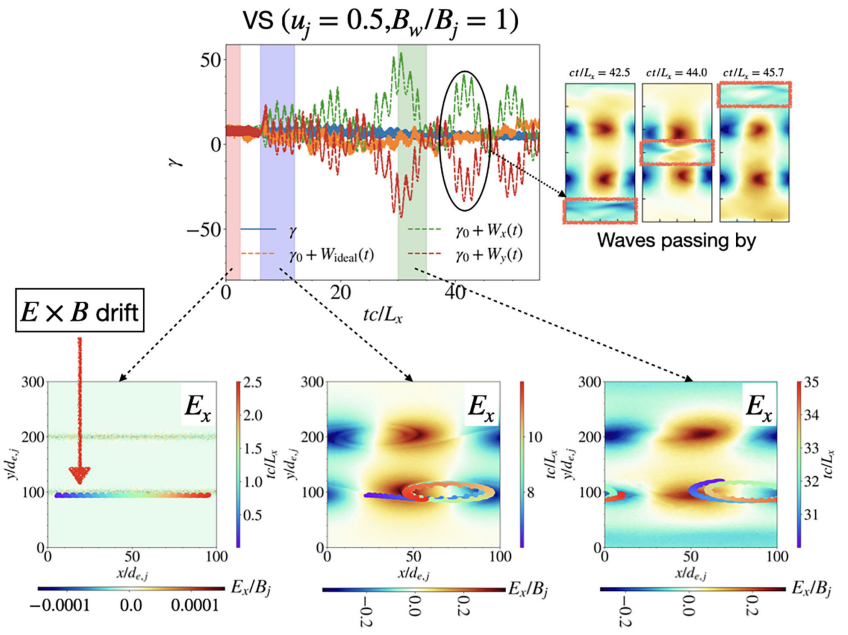

FIGURE 8. Energetics and trajectory of a particle in the VS case. The selected particle has a Lorentz factor of 10 at $tc/L_c = 27.3$. Top panel: Lorentz factor $\gamma(t)$ as a function of time (blue), in comparison with the work done by various components of the E field ($W_{\rm ideal}$, W_x, W_y, defined in the main text, representing the work done by the motional E_x and E_y fields). Bottom panels: trajectories of the particle at three time windows (marked by red, blue and green in the top panel), overlaid on three E_x snapshots taken at $tc/L_x = 0$, 8.75, 31.45. The panel on the top right, showing three E_x snapshots, displays the passage of waves (the passage of the wavecrest in the y direction is highlighted by the red rectangular boxes), which generates the large-scale bumps in the E_x, E_y work done.

the simulation, gaining no net energy. Beginning at $tc/L_x \approx 20$, some larger bumps appear in the E_x, E_y work done, with longer periodicity. This is due to waves passing by, as illustrated in the top-right panel, which lead to neither acceleration nor any substantial change in the particle's trajectory. Therefore, we did not investigate these waves further.

For the MS case (figure 9), we select a particle that has reached a Lorentz factor of 100 at $tc/L_x = 27.4$ for display, corresponding to the non-thermal tail in figure 7. As observed in the top panel, there is substantial increase in the Lorentz factor of this particle from 25 to 100. The increase in γ occurs in a single burst at $2.5 \leqslant tc/L_x \leqslant 4.5$, mainly due to the work done by the E_x component of the ideal motional E field. There is hardly any work done by the E_y component. In the bottom panels, we observe that the particle is initially performing a Speiser-like orbit close to the shear layer at $200d_{e,j}$ due to the B_z-field reversal. When DKI develops, the DK plumes bring plasma from both sides of the interface with the same E_x polarity into alignment, creating a channel that accelerates the particles linearly (Zenitani & Hoshino 2007). In the saturated stage, a thickened shear layer is created. The electromagnetic field within the thickened layer is drastically reduced, so particles simply pass through it ballistically. When the particle exits the shear layer, it resumes its Speiser-like orbit under the influence of the B field.

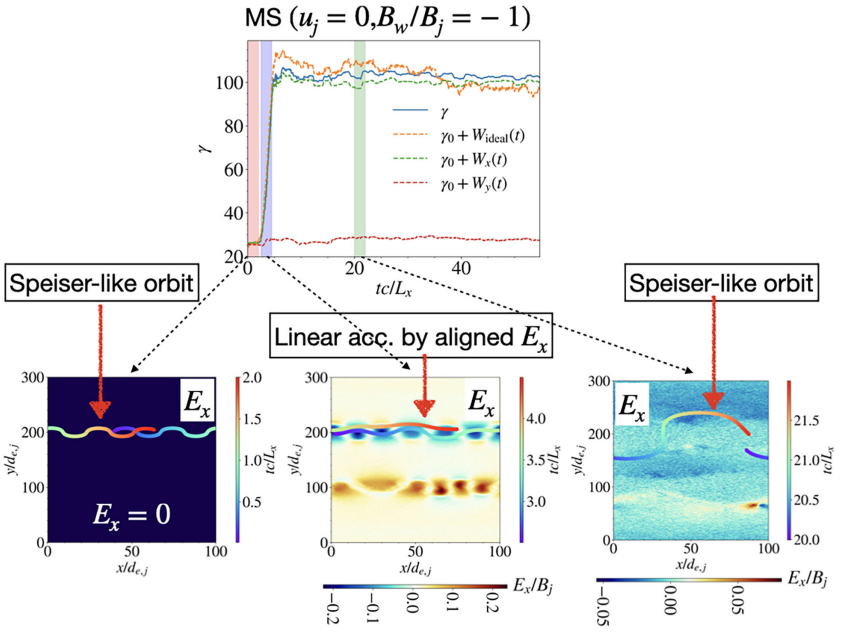

FIGURE 9. Energetics and trajectory of a particle in the MS case. The selected particle has a Lorentz factor of 100 at $tc/L_c = 27.3$. The meanings of the plots and legends are the same as in figure 8, with the difference that the trajectories in the bottom panels are taken at different times, and the E_x snapshots in the background are taken at $tc/L_x = 0$, 3.85, 21.1.

For the mixed-shear case ($u_j = 0.3$, $B_w/B_j = -1$; figure 10), we again select a particle that has reached a Lorentz factor of 100 at $tc/L_x = 27.4$ for display, corresponding to the non-thermal tail in figure 7. As observed in the top panel, there is substantial increase in the Lorentz factor of this particle from 35 to ~ 120. The increase in γ occurs in a stochastic manner, accumulating energy over an extended period of time. Most of the energy is gained over $12 \leqslant tc/L_x \leqslant 25$, mainly due to work done by the E_y component. This E_y arises from the motional field ($-\boldsymbol{v} \times \boldsymbol{B}$), which is non-zero due to the background fluid flow $v_x\hat{x}$ and magnetic field $B_z\hat{z}$. At the same time, E_x contributes very little to the overall increase in energy. In the bottom panels, we observe that the particle is initially performing a Speiser-like orbit (with a rather large radius of curvature), gradually shifting to an S-shaped trajectory in the nonlinear stage. Due to the moderately strong velocity shear in the background, the DK plumes are unable to align plasma with the same E_x polarity to produce a large-scale E_x channel; thus, we do not observe linear acceleration by E_x in the manner observed in the MS case. The background flow is substantially more turbulent than in the MS and VS cases, and the E_x field is also stochastic in appearance. In the top-right panel, we display the initial positions of the particles that underwent substantial acceleration, defined by acquiring a Lorentz factor above 30 by $tc/L_x = 27.4$, i.e. much higher than the mean $\bar{\gamma} \simeq 2.4$ corresponding to a thermal distribution with temperature $\theta = 1$. These particles are clustered initially at the shear interface, implying that they are likely accelerated there.

Figures 8–10 show that dissipation and particle acceleration in the single-shear cases (VS and MS, where there is only one kind of shear) are very different from those in the mixed-shear case. Specifically, in the mixed-shear case we uncovered a

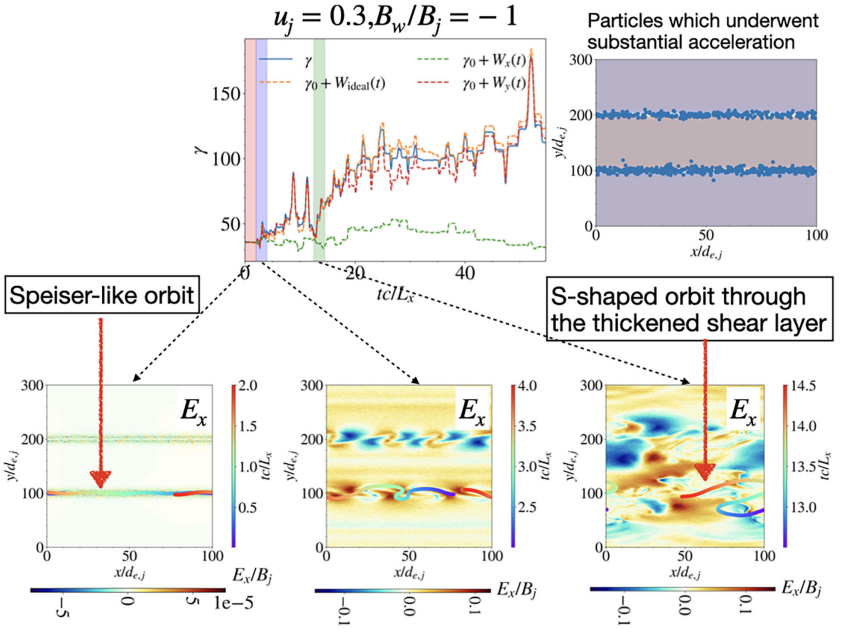

FIGURE 10. Energetics and trajectory of a particle in the mixed-shear ($u_j = 0.3$, $B_w/B_j = -1$) case. The selected particle has a Lorentz factor of 100 at $tc/L_c = 27.3$. The meanings of the plots and legends are the same as in figure 8, with the difference that the trajectories of the bottom panels are taken at different times, and the E_x snapshots in the background are taken at $tc/L_x = 0$, 3, 15.5. The top-right panel shows the initial positions of particles (blue dots) that were accelerated to $\gamma > 30$, superimposed on the initial B_z background.

new mechanism by which particles are accelerated mainly due to work done by E_y. This process is stochastic, with particle trajectories that exhibit a distinct S-shape. We illustrate the details of this type of acceleration in figure 11 by zooming in to the time period $12 \leqslant tc/L_x \leqslant 20$, where the particle acquires the greatest increase in γ. We observe an increase in γ from ≈ 40 to ≈ 90, acquired over four major jumps. Each jump is characterised by net positive work done by E_y. Focusing on jump 1 and jump 2, in the two top-right panels of figure 11 we plot the trajectories of the particle as it is energised, overlaid on the E_y-field background, with the colourbar indicating the strength of E_y. The trajectories are again rainbow-coloured to indicate the progress of time (blue, early; red, later). The thickened shear layer is clearly marked in orange in this colour scheme, and we observe $E_y \approx 0$ within the layer, so particles are not energised or de-energised by E_y as they pass through the layer. A finite $E_y < 0$ is present outside the shear layer, marked by blue, mainly due to the motional E field. During jump 1, the particle performs a U-shape turn, exiting the shear layer in the first half of the displayed trajectory and re-entering it in the second half. As the tracked particle is an electron and $E_y < 0$, there is a slight de-energisation as the particle exits the shear layer, going in the $-y$ direction. The electron quickly turns around due to B_z, going in the $+y$ direction, and is then energised before re-entering the shear layer. Due to the bent geometry of the shear layer, the particle covers a greater distance going upward than downward in the region with finite E_y (blue region), thus acquiring net energy. The same happens at jump 2, where the particle traverses a larger distance going upward than downward

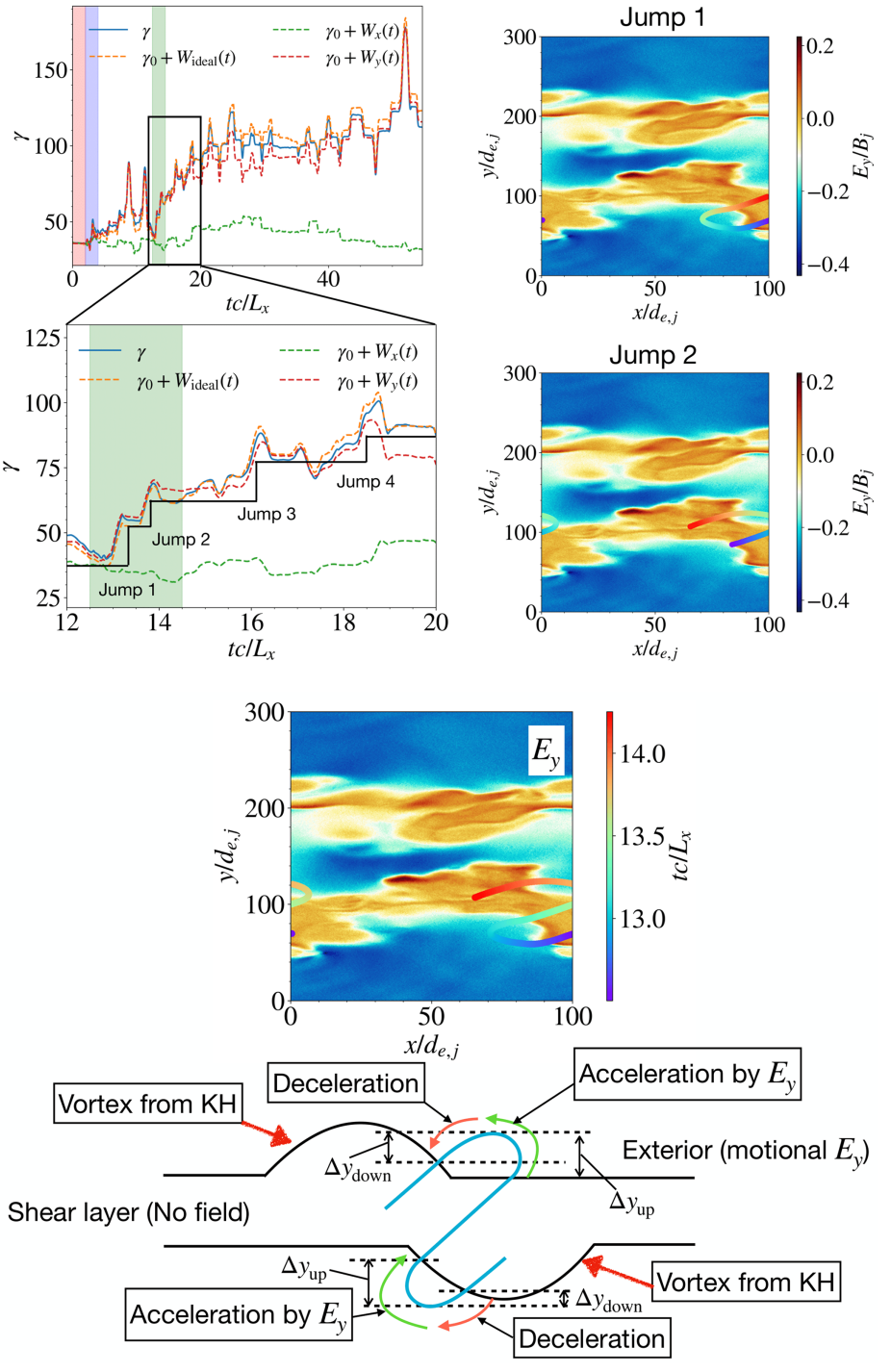

FIGURE 11. Top-left panels: zoom-in energetics of the selected particle over $12 \leqslant tc/L_x \leqslant 20$, illustrating the four jumps it took to acquire an increase in the Lorentz factor of ~ 50. Top-right panels: particle trajectories over jumps 1 and 2, overlaid on two E_y snapshots, with the colourbar indicating the strength of E_y. Bottom panels: particle trajectory over jumps 1 and 2 combined, with a schematic diagram showing how it is energised throughout the process.

in the region with finite E_y due to the bent geometry of the shear layer, thus acquiring net energy. This asymmetry between energisation and de-energisation of the particle in the motional E_y field, due to the bent geometry of the shear layer, leads to a gradual accumulation of energy and, thus, to particle acceleration. Combining the particle trajectories through jumps 1 and 2, we observe an S-shaped pattern, with the particle weaving in and out of the thickened shear layer.

We offer a simplified model of how particles are accelerated in the mixed-shear cases with the help of the schematic diagram at the bottom of figure 11. As shown in the diagram, a particle performs an S-shaped trajectory in and out of the shear layer due to the presence of a B_z field outside the shear. The particle streams through the shear layer ballistically as there is no field within it. Due to the bent geometry of the shear layer (depicted by the two lumps above and below the shear layer in the diagram), there is asymmetric energisation and de-energisation as work done is given by $\int \boldsymbol{E}_y \cdot \mathrm{d}\boldsymbol{l} \approx E_y(\Delta y_{\mathrm{up}} - \Delta y_{\mathrm{down}})$, where Δy_{up} and Δy_{down} are the upward and downward displacements of the particle as it weaves in and out of the bent shear layer (figure 11). If $\Delta y_{\mathrm{down}} < \Delta y_{\mathrm{up}}$ there will be a net energisation. On the other hand, if the shear layer were not bent (i.e. flat in the x direction, as in the saturated stage of the simulation, $tc/L_x \gtrsim 20$), then there would be equal energisation and de-energisation of the particle as it weaves in and out of it, resulting in no particle acceleration. The DKI and KHI both contribute to creating such a bent layer. In particular, DKI creates a shear layer where the electromagnetic field is suppressed, while KHI creates the vortical modulations which gives the layer a bent geometry; without either of them we would not have observed such particle acceleration. In Appendix D we show additional examples of particle acceleration through this mechanism, illustrating that the process described is not an isolated event.

The mechanism described, in which particles are accelerated due to asymmetric work done by the motional E_y external to the bent shear layer as they traverse an S-shaped orbit through it, is not the only way particles are accelerated, but accounts for particles at the highest end of the non-thermal spectrum. The histograms in figure 12 show contributions of the work done by E_x (green) and E_y (red), denoted by W_x, W_y, to the increase in the Lorentz factor $\Delta\gamma$, for tracked particles that have acquired $\gamma > 30$ (top left), $\gamma > 50$ (top right) and $\gamma > 70$ (bottom) at $tc/L_x = 27.4$. The angled brackets $\langle\cdot\rangle$ denote time average over $30 \leqslant tc/L_x \leqslant 50$. Thus, if a particle has a value of $\langle W_y\rangle/\langle\Delta\gamma\rangle \approx 1$, it means that all of the increase in γ is due to work done by E_y, and vice versa when this value is zero. Note that the ratio $\langle W_i\rangle/\langle\Delta\gamma\rangle$ can be greater than 1 or less than 0 as there could be net negative or positive work done by the other component of the electric field. We fit the histograms with a Gaussian $\exp[-(x-x_0)^2/2\sigma^2]$ and the fitted shifts x_0 are displayed. Observe that in all three panels, W_y contributes the majority to the increase in particle energy. The discrepancy between W_y and W_x, as shown by the difference in x_0, increases as we move to higher energy thresholds (from $\gamma > 30$ to $\gamma > 70$). In particular, for particles with $\gamma > 70$, W_y contributes 84 % of the energy gained while W_x contributes only 12 %. Thus, the mechanism described above accounts for most of the particle acceleration in the mixed-shear cases, particularly for the highest-energy particles.

The configuration depicted in the bottom panel of figure 11, where the particle exits and re-enters the shear layer with the slant direction as shown, favours net energisation of the particle. If the slant direction of the shear layer is different, net de-energisation may result. In figure 13 we describe when this happens. Focusing on a simplified picture where regions of possible acceleration/deceleration in a shear layer bent by the KHI–DKI interaction are modelled as diagonal strips

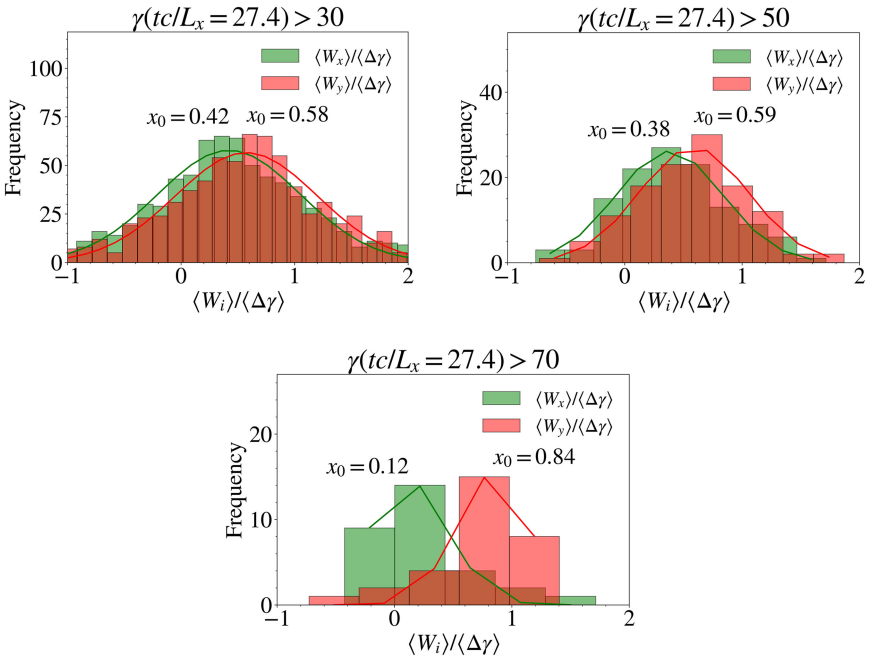

FIGURE 12. Histograms showing contributions of the work done by E_x (green) and E_y (red), denoted respectively by W_x and W_y (defined in § 3.2), to the increase in the Lorentz factor γ ($\Delta\gamma = \gamma - \gamma(t = 0)$), for tracked particles that have acquired $\gamma > 30$ (top left), $\gamma > 50$ (top right) and $\gamma > 70$ (bottom) at $tc/L_x = 27.4$. The histograms are fitted with a Gaussian $\exp[-(x - x_0)^2/2\sigma^2]$ and the fitted shifts x_0 are displayed. The angled brackets $\langle\cdot\rangle$ denote time average over $30 \leqslant tc/L_x \leqslant 50$.

(see top panel), we observe that the configuration in the middle-left panel, where the shear layer slants down from left to right, energises both electrons and positrons, while the other configuration, where the shear layer slants up from left to right, de-energises them. One can convince oneself that the direction the particle is travelling initially does not affect whether it is energised or de-energised – it is determined only by the slant direction of the shear layer. Thus, if particles (both electrons and positrons) encounter the configuration on the left more often than that on the right, net stochastic acceleration results. Intuitively, the slant length of the shear layer in the energising configuration will be stretched out due to the background shear, while in the de-energising configuration it will shrink (see bottom panel of figure 13). A larger slant length will likely expose the particles to more energising encounters, thus resulting in net energisation. We conclude this section with a remark that if one flips the orientation of the magnetic field while keeping the velocity field the same, the exterior motional electric field will flip in sign but the trajectories of the electrons and positions will reverse such that overall the energising configuration will remain energising and vice versa for the de-energising configuration.

4. Discussion and conclusion

In this study, we performed two-dimensional relativistic, collisionless pair-plasma PIC simulations of a thin layer subject to velocity and magnetic shear in the relativistically warm ($\theta = T/m_e c^2 \sim 1$) and moderately magnetised ($\sigma \sim 1$) regime.

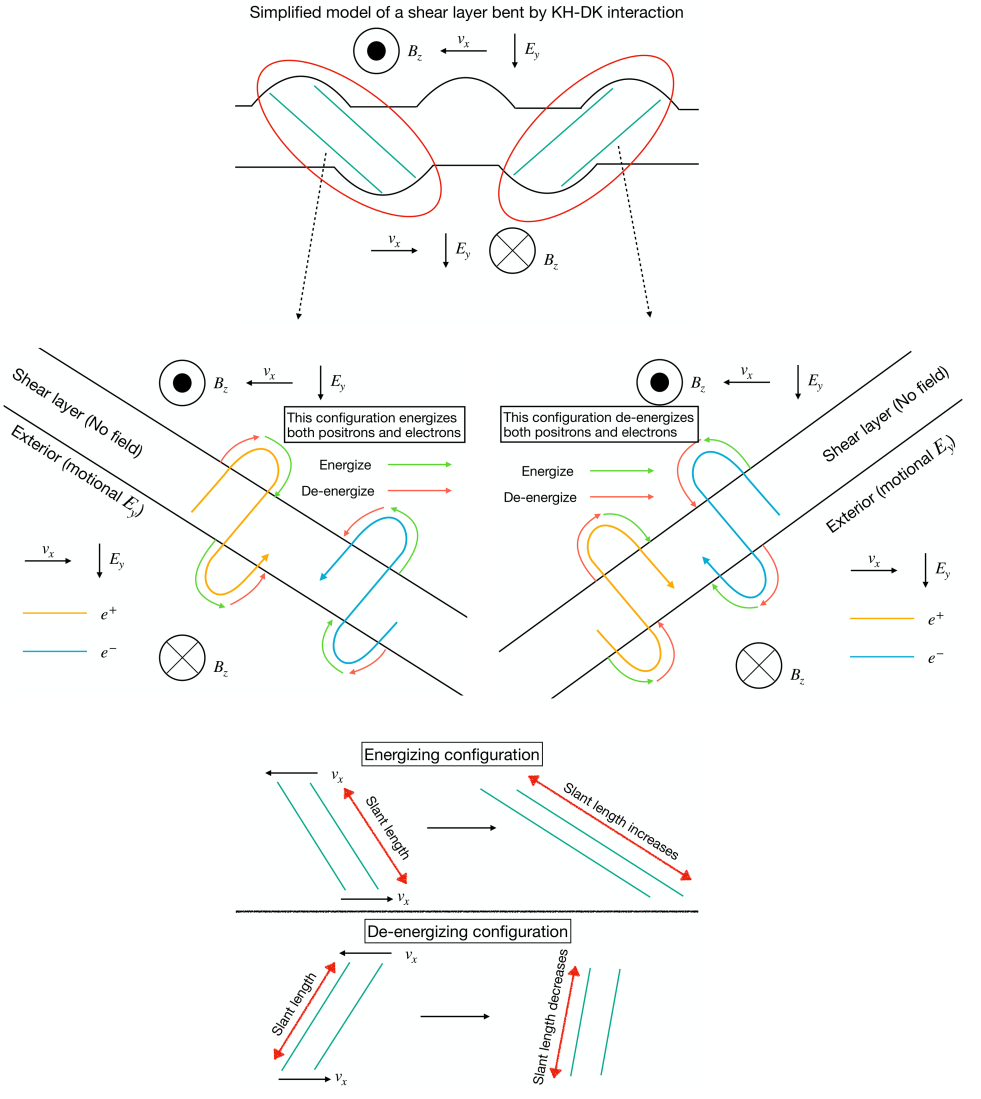

FIGURE 13. Top: simplified model of a shear layer bent by KHI–DKI interaction, where regions of possible acceleration/deceleration (circled in red) are modelled as slanted strips. Middle: depending on the orientation of the slanted strips (left: downwards from left to right; right: upwards from left to right), electrons and positrons can be net energised (left) or de-energised (right) due to asymmetric work done by the motional E_y field exterior to the shear layer. Bottom: the slant length of the strip in the energising configuration is stretched by background shear while it is shrunk in the de-energising configuration.

We created conditions where only the KHI and DKI can develop, while tearing modes are prohibited. By varying the magnitude of the velocity shear from zero to some supersonic value while keeping the magnetic field equal but opposite across the shear layer, we investigated the effects of velocity shear on DKI, including its nonlinear interplay with KHI. Our main findings are:

(i) The interaction of KHI and DKI creates qualitatively new flow structures compared with the cases that harbour only KHI or DKI: a thick, pressure-dominated shear layer with very weak electromagnetic field ('annihilated core'), modulated by KH vortices ('KH cocoon').

(ii) A moderate velocity shear ($u_j \leqslant 0.4$) has minimal effect on the linear growth of DK modes due to the lag between DK and KH growth times. For $u_j > 0.4$, the linear evolution is substantially modified, and no exponential growth phase can be captured.

(iii) The dissipation of magnetic energy and bulk kinetic energy varies drastically with velocity shear and depends sensitively on how strongly the KHI and DKI are excited. In the absence of velocity shear (MS case), DKI can dissipate a significant amount of magnetic energy. However, a weak shear ($u_j \leqslant 0.1$) disrupts DKI plumes and thus reduces dissipation. For moderately strong velocity shear ($0.2 \leqslant u_j \leqslant 0.4$), KHI becomes excited and KH vortices lead to a drastic rise in dissipation. Finally, for supersonic shear, KHI is weakened and we observe reduced dissipation. In the most dissipative case ($u_j = 0.3$), 40 % of the magnetic energy and 50 % of the bulk kinetic energy within the box are converted to internal energy while these numbers can be as low as 10 % for some other velocity shear values. We note that less than 5 % of the magnetic energy and nearly zero bulk kinetic energy are dissipated in the VS (purely KH) case. More details can be found in § 3.1 (figure 6).

(iv) We observe non-thermal power-law tails in the energy spectra of the mixed-shear cases, distinct from the MS (purely DK) and VS (purely KH) cases, thus suggesting different particle-acceleration mechanisms. By examining the trajectories and energisation histories of selected particles that have been accelerated, we find that in the MS case particles are accelerated linearly in a channel with aligned E_x (consistent with Zenitani & Hoshino (2007)) while in the mixed-shear case particles are stochastically accelerated by E_y in a shear layer bent by KHI–DKI interaction. This is a newly discovered way to accelerate particles.

(v) In this new acceleration mechanism, particles weave in and out of a bent shear layer in an S-shaped pattern due to the exterior magnetic field. They gain energy when the re-entry location is downstream/upstream (for positrons/electrons) of the exit location (relative to the exterior motional electric field) and lose energy in the opposite case. Whether a particle gains or loses energy is independent of the direction in which it is travelling – it depends only on the slant direction of the shear layer (as depicted in figure 13). The slant configuration that energises particles is more likely to be found than the opposite, thus leading to net acceleration.

(vi) Other acceleration mechanisms exist in the mixed-shear cases, but the new mechanism accounts for the majority of the particles accelerated and for the highest-energy particles found.

How are our results likely to scale with system size? Focusing on the most dissipative mixed-shear case ($u_j = 0.3$), we note that there is a high-energy cutoff in the particle energy spectrum at $\gamma \sim 300$. Is this cutoff intrinsic to the acceleration mechanism or due to limited system size? Note that for the assumed conditions in Zone j ($\theta_j = 1$, $\sigma_j = 1$), $d_{e,j} \sim \rho_{0,j}$, where $\rho_{0,j} = m_e c^2/eB_j$ is the nominal gyroradius. For relatively unchanged magnetic field exterior to the shear layer, the system size

can be cast as $L/\rho_{0j} \sim L/d_{e,j} \sim 100$. The Hillas energy limit, which is defined as $\gamma_{\max} = L/\rho_{0j}$, is then ~ 100, comparable to the observed spectral cutoff. The high-energy cutoff is thus likely due to the system-size limit, which suggests that the non-thermal power-law tail in the mixed-shear case will likely extend further with a larger box size. It follows that in astrophysical settings particles can be accelerated to well beyond $\gamma \sim 10^2$. We relegate a detailed examination of system-size scaling to future work.

In this study we explored only a relativistically warm, moderately magnetised pair plasma in two dimensions, varying the velocity shear while holding magnetic shear constant. We also restricted our consideration to KHI and DKI, leaving out tearing modes.[4] Many possible follow-up studies can be devised, for example by varying the initial orientation of the magnetic field ($\boldsymbol{B} = B_z\hat{z} \rightarrow \boldsymbol{B} = B(\cos\theta\hat{x} + \sin\theta\hat{z})$) so as to introduce tearing modes into the problem. One can also investigate how the results translate to a normal ($e-p$) plasma and across a range of temperatures and magnetisations. Ultimately, the aim is to generalise our understanding of the problem from two to three dimensions. This study, therefore, should be viewed as only the first step towards a comprehensive understanding of dissipation and particle acceleration at intermittent structures which harbour both velocity and magnetic shears.

The shear layers with which we initiate our set-up are marked by spatially coincident vortex and current sheets with the same thickness. While this is a simplifying assumption, Jain *et al*. (2021) and Hubbert *et al*. (2021) have shown that kinetic-scale current sheets are tightly correlated with electron shear-flow structures, at least in non-relativistic, $e-p$ plasma turbulence. In fact, thin vortex and current sheets have separately been found to be characteristics of intermittency in turbulence, and responsible for a substantial amount of dissipation (Zhdankin *et al*. 2016). A detailed examination of the alignment and magnitudes of current and vortex sheets at intermittent structures, in simulations of MHD turbulence, would offer us a clearer picture of the most relevant configurations for future simulations.

Our results are relevant to a range of astrophysical settings because of the ubiquity of plasma turbulence. In low-energy settings, dissipation at intermittent structures has often been associated with nanoflares, X-ray bursts in the solar corona and wind (Dmitruk & Gómez 1997; Dmitruk, Gómez & DeLuca 1998). Recent studies have begun to see intermittent structures as the means by which cosmic rays in galaxies are scattered and transported (Kempski *et al*. 2023; Lemoine 2023). In high-energy settings, intermittent heating could be responsible for flares observed in black-hole accretion flows (Giannios 2012; Ripperda, Bacchini & Philippov 2020), limb brightening at active galactic nucleus jet boundaries (Duran, Tchekhovskoy & Giannios 2016; Sridhar *et al*. 2025), rapid variability in gamma-ray bursts (Drenkhahn & Spruit 2002) and other phenomena, thus highlighting the need for further investigation of the nonlinear interactions of multiple instabilities, sourced from magnetic and velocity shears, at the kinetic level.

[4] During the review process, our attention was drawn to a new instability that could be triggered in such systems, namely the electron Rayleigh–Taylor instability (ERTI) (Che 2025), which operates under a principle similar to that of the Rayleigh–Taylor instability except that the potential field is now generated by the motional electric field in the in-plane (y) direction due to an out-of-plane (z) magnetic field and bulk plasma flow in the x direction, conditions which are aligned with our set-up. The ERTI requires a density difference across the shear layer, and generates unstable modes with wavevector pointing out of plane. As there is no density contrast across the shear layer in our set-up, and the out-of-plane wavenumber is unresolved in two dimensions, the ERTI is not a concern in this study. However, in future studies the orientation of the magnetic field will be varied and density differences across the shear layer will be introduced. Consideration of ERIT will likely be crucial when we perform three-dimensional simulations in forthcoming studies.

Acknowledgements

We thank L. Sironi, V. Zhdankin and N. Sridhar for useful comments and suggestions. We are also grateful for the comments and suggestions made by the anonymous reviewers, which improved the manuscript significantly. This work is supported by NASA Astrophysics Theory Program grants 80NSSC22K0828 and 80NSSC24K0941, and ACCESS computing grants PHY140041 and PHY240194.

Editor Thierry Passot thanks the referees for their advice in evaluating this article.

Declaration of interests

The authors report no conflict of interest.

Appendix A. Details of the model set-up

Our set-up is based on the one described in Rowan (2019) and is a relativistic modification of the Harris sheet (Harris 1962; Kirk & Skjæraasen 2003) taking into account the bulk plasma flow. Due to velocity and magnetic shears, there are current and charge excesses at the shear interfaces, which imply that the electron and positron densities and bulk velocities will be different close to the interfaces. Therefore, when we mention quantities with the subscripts 'j' or 'w' we are referring to their values far from the interfaces, in the respective Zone j and Zone w regions where the current and charge excess are zero. There, the bulk speeds and rest-frame electron and positron densities are equal: $\beta_{e,j} = \beta_{p,j}$, $\beta_{e,w} = \beta_{p,w}$ and $\tilde{n}_{e,j} = \tilde{n}_{p,j}$, $\tilde{n}_{e,w} = \tilde{n}_{p,w}$.

Assuming equal jet rest-frame electron and positron temperatures, $\theta_{e,j} = \theta_{p,j} \equiv \theta_j$, the rest-frame mean particle speed $\bar{v}_j$ in Zone j (and the mean Lorentz factor $\bar{\gamma}_j$) for a given jet temperature θ_j can be determined from the local Maxwell–Jüttner distribution. The adiabatic index $\Gamma_{\rm ad}(\theta_j)$ of the electrons and positrons can be found using the fitting formula given by (14) in Service (1986). Together, $\bar{\gamma}_j$ and the rest-frame jet electron (and positron) particle density $\tilde{n}_{e,j} = \tilde{n}_{p,j} = \tilde{n}_{e,j}$ define the main normalising length scale in our simulations: the electron inertial length $d_{e,j} \equiv c/\omega_{pe,j}$, where $\omega_{pe,j} \equiv (4\pi \tilde{n}_{e,j} e^2/\bar{\gamma}_j m_e)^{1/2}$ is the comoving electron plasma frequency. The comoving jet enthalpy density, which enters the expression for magnetisation σ_j, is given by $w_j = w_{e,j} + w_{p,j} = 2[1 + \Gamma_{{\rm ad},j}/(\Gamma_{{\rm ad},j} - 1)\theta_j]\tilde{n}_{e,j} m_e c^2$.

The plasma bulk velocity $\beta_x(y)$ and the magnetic field are initialised with the following profiles:

$$\beta_x(y) = \beta_j \left[1 - \tanh\left(\frac{y - y_1}{\Delta}\right) + \tanh\left(\frac{y - y_2}{\Delta}\right)\right], \tag{A1}$$

$$B_z(y) = B_j \left\{\frac{B_w}{B_j} + \frac{1}{2}\left(1 - \frac{B_w}{B_j}\right)\left[\tanh\left(\frac{y - y_1}{\Delta}\right) - \tanh\left(\frac{y - y_2}{\Delta}\right)\right]\right\}, \tag{A2}$$

where $\beta_j = u_j/(1 + u_j^2)^{1/2}$ is the velocity of Zone j (normalised by c) corresponding to the specified normalised 4-velocity u_j; y_1, y_2 are the y locations of the shear interfaces; and Δ is the half-width of the shear (and also current) layer at these interfaces. The initial laboratory-frame electric field, current density and charge density are given by $\boldsymbol{E} = -\boldsymbol{v} \times \boldsymbol{B}/c = \beta_x B_z \hat{y}$, $\boldsymbol{J} = c\mathrm{d}B_z y/4\pi \hat{x}$ and $\rho_e = (\mathrm{d}E_y y)/4\pi$, as dictated by the ideal MHD Ohm's law, Ampere's law, and Gauss's law, respectively.

The y profiles of the laboratory-frame electron and positron number densities n_e, n_p and of the bulk velocities $\beta_{e,x}, \beta_{p,x}$ are constrained to satisfy the self-consistency conditions

$$\rho_e = \left(n_p - n_e\right) e, \tag{A3}$$

$$J_x = \left(n_p \beta_{p,x} c - n_e \beta_{e,x}\right) ec, \tag{A4}$$

$$\beta_x = \frac{n_p \beta_{p,x} + n_e \beta_{e,x}}{n_p + n_e}. \tag{A5}$$

To proceed, we recast n_p, n_e as

$$n_p = n_0 \left(1 - \delta_n\right), \quad n_e = n_0 \left(1 + \delta_n\right), \tag{A6}$$

where $n_0 = \Gamma(y)\tilde{n}_0$ can be regarded as some background laboratory-frame density profile. The bulk Lorentz-factor profile is given by $\Gamma(y) = 1/(1 - \beta_x^2)^{1/2}$, and the rest-frame background density $\tilde{n}_0$ by

$$\tilde{n}_0(y) = \tilde{n}_{e,j} \left\{ \frac{\tilde{n}_{e,w}}{\tilde{n}_{e,j}} + \frac{1}{2} \left(1 - \frac{\tilde{n}_{e,w}}{\tilde{n}_{e,j}}\right) \left[\tanh\left(\frac{y - y_1}{\Delta}\right) - \tanh\left(\frac{y - y_2}{\Delta}\right) \right] \right\}. \tag{A7}$$

In this study, for simplicity we take the rest-frame jet and wind density to be the same, $\tilde{n}_{e,w}/\tilde{n}_{e,j} = 1$. Substituting (A6) into (A3)–(A5) and solving, we then have

$$\delta_n = -\frac{\rho_e}{2n_0 e}, \tag{A8}$$

$$\beta_{e,x} = \frac{2n_0 e\beta_x - J_x/c}{2n_0(1 + \delta_n)e}, \quad \beta_{p,x} = \frac{2n_0 e\beta_x + J_x/c}{2n_0(1 - \delta_n)e}. \tag{A9}$$

Finally, to determine the electron and positron temperature profiles $\theta_{e,p}(y)$, we employ pressure balance:

$$\tilde{n}_p m_e c^2 \theta_p + \tilde{n}_e m_e c^2 \theta_e + \frac{B_z^2}{8\pi \Gamma^2} = \text{const.} \tag{A10}$$

Assuming $\theta_p(y) = \theta_e(y)$ initially, these temperatures can be determined from (A10). The temperature profiles of the positrons and electrons are doubly peaked, with temperature away from the layer equal to θ_j, and peaking at the layer centres (where the magnetic field is zero initially) to maintain pressure balance across. This completes the PIC set-up of the model.

Appendix B. Definition of the plasma microscales

The key plasma length scales describing our system are the initial jet electron inertial length $d_{e,j} \equiv c/\omega_{pe,j}$, where $\omega_{pe,j} \equiv (4\pi \tilde{n}_{ej} e^2/\bar{\gamma}_j m_e)^{1/2}$ is the plasma frequency ($\tilde{n}_{e,j}$ is the rest-frame jet electron number density and $\bar{\gamma}_j$ is the mean Lorentz factor of Zone j's rest-frame Maxwell–Jüttner distribution), Zone j's electron Debye length $\lambda_{De} \equiv (T_j/4\pi n_{e,j} e^2)^{1/2} \sim \theta_j^{1/2} d_{e,j}$ and the characteristic jet electron gyroradius $\rho_j \equiv \bar{\gamma}_j m_e \bar{v}_j c/eB_j \sim (\theta_j/\sigma_j)^{1/2} d_{e,j}$ (where $\bar{v}_j$ is the mean particle velocity). For relativistically warm ($\theta \sim 1$), moderately magnetised ($\sigma \sim 1$) plasma the three plasma length scales ($d_{e,j}$, λ_{De}, ρ_j) are roughly equal.

Appendix C. Decomposing the stress tensor into thermal and bulk components

We describe the procedure for decomposing the stress tensor into thermal and bulk-flow components, needed to monitor the bulk kinetic energy content. We thank V. Zhdankin (personal communication) for offering insights on this procedure.

The procedure is as follows:

1. For each species s, calculate the number density $n = \sum_l w_l/\Delta V$, the stress tensor $\Pi_{ij} = \sum_l \gamma_l m_{s,l} w_l v_{l,i} v_{l,j}/\Delta V$, momentum density $U_{p,i} = \sum_l \gamma_l m_{s,l} w_l v_{l,i}/\Delta V$, energy density $U_e = \sum_l \gamma_l w_l m_{s,l} c^2/\Delta V$ and particle flux $F_i = \sum_l w_l v_{l,i}/\Delta V$ at each grid point, where the sum is taken over all (macro)particles in the neighbourhood of a cell, w_l is the weight of the macroparticles, γ_l is their Lorentz factor, $m_{s,l}$ is the particle mass, ΔV is the volume element and $v_{l,i}$ is the i component of the particle's velocity. These laboratory-frame quantities are outputted automatically in Zeltron.

2. Rotate the laboratory-frame vector and tensor quantities $\boldsymbol{U}_p$, $\boldsymbol{F}$, $\boldsymbol{\Pi}$ to the frame x', y', z' such that the particle flux $\boldsymbol{F}'$ points in the x' direction. Note that scalar quantities such as U_e, n are rotationally invariant.

3. The components of the comoving thermal pressure tensor in the rotated frame can be obtained by the following equations:

$$\begin{aligned}
P'_{x'x'} &= \Gamma_b^2 \left(\Pi'_{x'x'} - 2v_b U'_{p,x'} + (v_b/c)^2 U_e\right), \\
P'_{x'y'} &= \Gamma_b \left(\Pi'_{x'y'} - v_b U'_{p,y'}\right), \\
P'_{x'z'} &= \Gamma_b \left(\Pi'_{x'z'} - v_b U'_{p,z'}\right), \\
P'_{y'y'} &= \Pi'_{y'y'}, \\
P'_{y'z'} &= \Pi'_{y'z'}, \\
P'_{z'z'} &= \Pi'_{z'z'},
\end{aligned} \tag{C1}$$

   where $v_b = F'_{x'}/n$ is the bulk speed of the Eckart frame (the frame for which particle flux is zero) and $\Gamma_b = (1 - v_b^2/c^2)^{-1/2}$.

4. Inverse-rotate $P'_{i'j'}$ to obtain the thermal pressure tensor P_{ij} in the laboratory frame. The bulk-flow dynamic pressure can be obtained by subtracting P_{ij} from Π_{ij} (i.e. $P_{b,ij} = \Pi_{ij} - P_{ij}$). These are then the thermal and dynamic pressure tensors for species s.

5. The total bulk-flow kinetic and thermal energies can then be obtained by taking the trace of the respective pressure tensors over all volume $\sum_V \sum_i P_{b,ii} \Delta V$ and $\sum_V \sum_i P_{ii} \Delta V$, for all species present.

The justification for the procedure is as follows. First, note that thermal pressure is defined in the bulk frame of the plasma:

$$P_{ij} = \int \mathrm{d}^3 \bar{\boldsymbol{p}} \bar{f} \bar{\gamma} m_s \bar{v}_i \bar{v}_j, \tag{C2}$$

with barred quantities denoting comoving-frame quantities. Here, $\bar{f}(\bar{\boldsymbol{x}}, \bar{\boldsymbol{p}}, \bar{t})$ is the distribution function satisfying $\bar{n} = \int \mathrm{d}^3 \bar{\boldsymbol{p}} \bar{f}$. The comoving frame is connected to the laboratory (or simulation) frame (denoted by unbarred quantities) by the Lorentz transformation corresponding to the bulk velocity $\boldsymbol{v}_b$ and the associated Lorentz

factor $\Gamma_b = (1 - v_b^2/c^2)^{-1/2}$. We do not specify $\boldsymbol{v}_b$ for now to keep this derivation general. Using the Jacobian of the Lorentz transformation matrix and the fact that particle number is invariant with respect to frame transformation, we have $\mathrm{d}^3\boldsymbol{p}/\gamma = \mathrm{d}^3\bar{\boldsymbol{p}}/\bar{\gamma}$ and $f = \bar{f}$. This gives

$$\int \mathrm{d}^3\bar{\boldsymbol{p}}\,\bar{f}\bar{\gamma}m_s\bar{v}_i\bar{v}_j = \int \mathrm{d}^3\boldsymbol{p}\frac{\bar{\gamma}}{\gamma}f\bar{\gamma}m_s\bar{v}_i\bar{v}_j = \int \mathrm{d}^3\boldsymbol{p}\frac{f}{\gamma m_s}\bar{p}_i\bar{p}_j. \tag{C3}$$

If we assume the bulk motion is entirely in the x direction, $\boldsymbol{v}_b = v_b\hat{x}$ (if it were not, one could simply rotate into a frame in which it is), then Lorentz transformation of the 4-momentum gives $\bar{p}_x = \Gamma_b(p_x - v_bE/c^2)$, $\bar{p}_y = p_y$, $\bar{p}_z = p_z$. Substituting into (C3) and noting that $\Pi_{ij} = \int \mathrm{d}^3\boldsymbol{p}f\gamma m_s v_i v_j$, $U_{p,i} = \int \mathrm{d}^3\boldsymbol{p}f\gamma m_s v_i$, $U_e = \int \mathrm{d}^3\boldsymbol{p}f\gamma m_s c^2$ in the continuous limit gives the equations listed in point (iii) of the procedure. Unlike the prescription described in Zhdankin (2021), we have selected the bulk frame to be the zero-particle-flux frame (Eckart's frame), $v_b = F_x/n$.

Appendix D. Additional examples of particle acceleration by the new mechanism in the mixed-shear $u_j = 0.3$ case

In figures 14 and 15 we show two more examples of particle acceleration through the new mechanism described in § 3.2, i.e. asymmetric work done by the motional E_y as a particle performs S-shaped orbits through a bent shear layer, acquiring net energisation. In figure 14 we select a particle that has reached a Lorentz factor

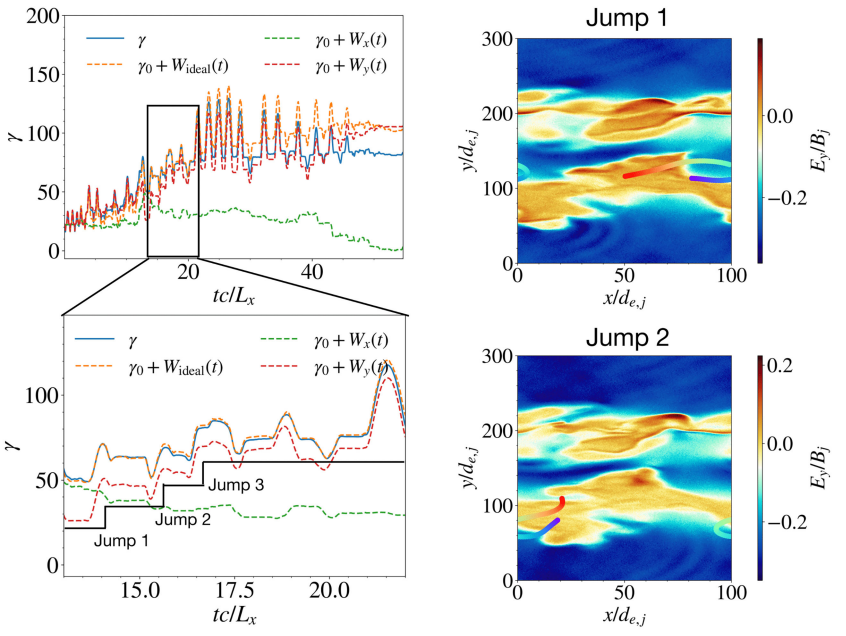

FIGURE 14. Left: particle energetics of a selected particle (electron) that has reached a Lorentz factor of $\gamma = 95$ at $tc/L_x = 27.4$ in the $u_j = 0.3$ mixed-shear case, with a zoom-in panel focusing on the time period $13 \leqslant tc/L_x \leqslant 22$. Terms W_{ideal}, W_x, W_y are defined in the main text in § 3.2. Right: trajectories of the particle over two time windows, corresponding to jumps 1 and 2 indicated in the lower-left panel, overlaid on an E_y snapshot. Colourbar indicates the strength of E_y, while the rainbow-coloured trajectories indicate the progress of time (blue, early; red, later).

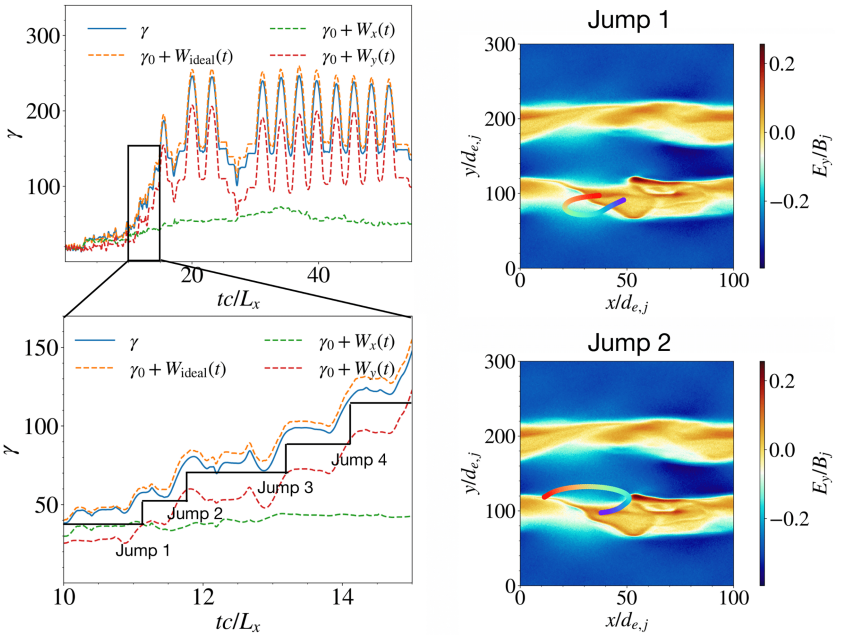

FIGURE 15. Same as in figure 14 but for a particle (electron) that has reached a Lorentz factor of $\gamma = 105$ at $tc/L_x = 27.4$.

$\gamma = 95$ at $tc/L_x = 27.4$, while in figure 15 we select a particle that has reached a Lorentz factor $\gamma = 105$ at $tc/L_x = 27.4$. In both figures, we show the S-shaped orbits performed by the particles over two time windows, corresponding to jumps 1 and 2 indicated in the lower-left panel, where the particle acquires net energisation from the work done by E_y.

REFERENCES

BARKOV, M.V. & KOMISSAROV, S.S. 2016 Relativistic tearing and Drift–Kink instabilities in two-fluid simulations. *MNRAS* **458**, 1939–1947.

CERUTTI, B., WERNER, G.R., UZDENSKY, D.A. & BEGELMAN, M.C. 2013 Simulations of particle acceleration beyond the classical synchrotron burnoff limit in magnetic reconnection: an explanation of the crab flares. *ApJ* **770**, 147.

CHE, H. 2025 Impact of transverse magnetic field on electromagnetic electron Kelvin–Helmholtz instability and a new electron Rayleigh–Taylor instability. *Phys. Plasmas* **32**, 062108.

CHE, H. & ZANK, G.P. 2023 Electromagnetic electron Kelvin–Helmholtz instability. *Phys. Plasmas* **30**, 062110.

CHOW, A., ROWAN, M.E., SIRONI, L., DAVELAAR, J., BODO, G. & NARAYAN, R. 2023 Linear analysis of the Kelvin–Helmholtz instability in relativistic magnetized symmetric flows. *MNRAS* **524**, 90–99.

DAUGHTON, W. 1999 Two-fluid theory of the drift kink instability. *JGR* **104**, 28701–28708.

DMITRUK, P. & GÓMEZ, D. 1997 Turbulent coronal heating and the distribution of nanoflares. *ApJL* **484**, L83—L86.

DMITRUK, P., GÓMEZ, D. & DELUCA, E. 1998 Magnetohydrodynamic turbulence of coronal active regions and the distribution of nanoflares. *ApJ* **505**, 974–983.

DRENKHAHN, G. & SPRUIT, H. 2002 Efficient acceleration and radiation in poynting flux powered grb outflows. *Astron. Astrophys.* **391**, 1141–1153.

DURAN, R., TCHEKHOVSKOY, A. & GIANNIOS, D. 2016 Simulations of agn jets: magnetic kink instability versus conical shocks. *MNRAS* **469**, 4957–4978.

GIANNIOS, D. 2012 Reconnection-driven plasmoids in blazars: fast flares on a slow envelope. *MNRAS* **431**, 355–363.

GUO, F., LI, H., DAUGHTON, W. & LIU, Y.-H. 2014 Formation of hard power laws in the energetic particle spectra resulting from relativistic magnetic reconnection. *Phys. Rev. Lett.* **113**, 155005.

HARRIS, E.G. 1962 On a plasma sheath separating regions of oppositely directed magnetic field. *Il Nuovo Cimento* **23**, 115–121.

HUBBERT, M., QI, Y., RUSSELL, C.T., BURCH, J.L., GILES, B.L. & MOORE, T.E. 2021 Electron only tail current sheets and their temporal evolution. *GeoRL* **48**, e91364.

JAIN, N., BÜCHNER, J., COMIŞEL, H. & MOTSCHMANN, U. 2021 Free energy sources in current sheets formed in collisionless plasma turbulence. *ApJ* **919**, 103.

KEMPSKI, P., FIELDING, D.B., QUATAERT, E., GALISHNIKOVA, A.K., KUNZ, M.W., PHILIPPOV, A.A. & RIPPERDA, B. 2023 Cosmic ray transport in large-amplitude turbulence with small-scale field reversals. *MNRAS* **525**, 4985–4998.

KIRK, J.G. & SKJÆRAASEN, O. 2003 Dissipation in poynting-flux-dominated flows: the σ-problem of the crab pulsar wind. *ApJ* **591**, 366–379

LEMOINE, M. 2023 Particle transport through localized interactions with sharp magnetic field bends in MHD turbulence. *J. Plasma Phys.* **89**, 175890501.

PRITCHETT, P.L., CORONITI, F.V. & DECYK, V.K. 1996 Three-dimensional stability of thin quasi-neutral current sheets. *JGR* **101**, 27413–27430.

RIPPERDA, B., BACCHINI, F. & PHILIPPOV, A. 2020 Magnetic reconnection and hot spot formation in black hole accretion disks. *ApJ* **900**, 100.

ROWAN, M.E. 2019 Dissipation of magnetic energy in collisionless accretion flows. PhD thesis, Harvard University.

SERRANO, R.F., NÄTTILÄ, J. & ZHDANKIN, V. 2024 Scale statistics of current sheets in relativistic collisionless plasma turbulence. arXiv: 2408.12511.

SERVICE, A.T. 1986 Fitting formulae for the equation of state of a perfect, semirelativistic Boltzmann gas. *ApJ* **307**, 60.

SIRONI, L., ROWAN, M.E. & NARAYAN, R. 2021 Reconnection-driven particle acceleration in relativistic shear flows. *ApJ Lett.* **907**, L44.

SIRONI, L., UZDENSKY, D.A. & GIANNIOS, D. 2025 Relativistic magnetic reconnection in astrophysical plasmas: a powerful mechanism of nonthermal emission. *ARA&A* **63**, 127–178.

SRIDHAR, N., RIPPERDA, B., SIRONI, L., DAVELAAR, J. & BELOBORODOV, A.M. 2025 Bulk motions in the black hole jet sheath as a candidate for the comptonizing corona. *ApJ* **979**, 199.

WERNER, G.R. & UZDENSKY, D.A. 2021 Reconnection and particle acceleration in three-dimensional current sheet evolution in moderately magnetized astrophysical pair plasma. *J. Plasma Phys.* **87**, 905870613.

WERNER, G.R., UZDENSKY, D.A., CERUTTI, B., NALEWAJKO, K. & BEGELMAN, M.C. 2016 The extent of power-law energy spectra in collisionless relativistic magnetic reconnection in pair plasmas. *ApJ Lett.* **816**, L8.

ZENITANI, S. & HOSHINO, M. 2007 Particle acceleration and magnetic dissipation in relativistic current sheet of pair plasmas. *ApJ* **670**, 702–726.

ZENITANI, S. & HOSHINO, M. 2008 The role of the guide field in relativistic pair plasma reconnection. *ApJ* **677**, 530–544.

ZHDANKIN, V. 2021 Particle energization in relativistic plasma turbulence: solenoidal versus compressive driving. *ApJ* **922**, 2106–00743.

ZHDANKIN, V., BOLDYREV, S. & UZDENSKY, D.A. 2016 Scalings of intermittent structures in magneto-hydrodynamic turbulence. *Phys. Plasmas* **23**, 055705.

ZHU, Z. & WINGLEE, R.M. 1996 Tearing instability, flux ropes, and the kinetic current sheet kink instability in the Earth's magnetotail: a three-dimensional perspective from particle simulations. *JGR* **101**, 4885–4898.